Transient dynamics in the outflow of energy from a system in a nonequilibrium stationary state

Paweł J. Żuk [ORCID],[1,2,*] Karol Makuch [ORCID],[1] Robert Hołyst [ORCID],[1,†] and Anna Maciołek [ORCID][1,3,‡]

[1]*Institute of Physical Chemistry, Polish Academy of Sciences, Kasprzaka 44/52, PL-01-224 Warsaw, Poland*
[2]*Department of Physics, Lancaster University, Lancaster LA1 4YB, United Kingdom*
[3]*Max-Planck-Institut für Intelligente Systeme Stuttgart, Heisenbergstrasse 3, D-70569 Stuttgart, Germany*

We investigate the thermal relaxation of an ideal gas from a nonequilibrium stationary state. The gas is enclosed between two walls, which initially have different temperatures. After making one of the walls adiabatic, the system returns to equilibrium. We notice two distinct modes of heat transport and associated timescales: one connected with a traveling heat front and the other with internal energy diffusion. At the heat front, which moves at the speed of sound, pressure, temperature, and density change abruptly, leaving lower values behind. This is unlike a shock wave, a sound wave, or a thermal wave. The front moves multiple times between the walls and is the dominant heat transport mode until surpassed by diffusion. We found that it can constitute an order 1 factor in shaping the dynamics of the outflow of internal energy. We found that cooling such a system is quicker than heating, and that hotter bodies cool down quicker than colder ones. The latter is known as the Mpemba effect.

I. INTRODUCTION

According to Fourier's law, a temperature gradient induces heat flow [1–5]. Most heat transport studies (if convection and radiation are neglected) are based on the parabolic equation of heat diffusion, which is a consequence of Fourier's law [6]. However, this theoretical framework cannot always describe heat transfer in a very small scale of time and space. For fast processes where the response of the medium takes place on a similar timescale to the energy transport, thermal waves can be generated [7–12]. In such situations, there will be a time delay between the appearance of the temperature gradient and the establishment of the heat flux, resulting in an oscillatory relaxation. When it comes to small lengthscales, e.g., if the sample is smaller than or comparable to the mean free path of phonons or particles [13], ballistic heat transport can take place, leading to an increase in heat flux [14–16]. Even more possibilities of energy transport are encountered in a compressible fluid. There, the energy can be transported via sound waves [17,18], where the alternating contractions and retractions of gas move at the speed of sound, carrying the kinetic energy of the oscillating movement of the gas and the associated changes in the internal energy. Shock waves can also propagate in compressible fluids [18–20]. These are moving surfaces of discontinuity of the thermodynamic parameters (pressure, density, temperature, entropy) with a gas velocity normal to the surface.

In the present paper, we uncover still another mode of heat transport by considering a macroscopic system: an ideal gas confined between two planar walls. Initially, the gas is in a nonequilibrium stationary state due to different temperatures at the two walls. The relaxation process begins as one wall suddenly becomes adiabatic (the temperature gradient on that wall is set to zero). Using the laws of conservation of mass, momentum, and energy [21], we study the flow of the internal energy inside the system and into the surroundings in response to this sudden change. Interestingly, we discover that if the hotter wall is set adiabatic, up to 10% of internal energy is removed from the system via the front moving at the local speed of sound and against the pressure gradient. This front reflects from the walls multiple times, and during each passage the system's internal energy is lowered by a quantized amount. Moreover, we find the asymmetry between relaxation to equilibrium via cooling or heating, i.e., cooling after the hotter wall becomes adiabatic progresses faster than heating after the colder wall becomes adiabatic. For an otherwise identical system, the one with a higher initial temperature at the hotter wall cools down quicker. We argue that this accelerated cooling and the observed asymmetry of relaxation are a consequence of the relationship between the amount of energy stored in the steady state and the heat flux flowing through the system in this state. The quicker cooling from the hotter system is known as the "Mpemba effect" [22,23]. In the case of microscopic systems, the Mpemba effect was demonstrated both experimentally and theoretically [24–29]. The crucial difference here is that the systems considered in Refs. [24–29] were initialized in a state that was thermally equilibrated, whereas we initialize the system in the nonequilibrium steady state where heat flux is present. Another interesting example of the importance of initial conditions in relaxation has been recently found in systems undergoing reversible

---

*pzuk@ichf.edu.pl
†rholyst@ichf.edu.pl
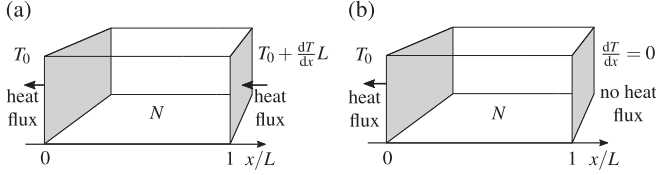‡amaciolek@ichf.edu.pl

FIG. 1. The model. (a) Initial conditions are set by the nonequilibrium stationary state. (b) Boundary conditions out of a nonequilibrium stationary state.

overdamped diffusion in single-well potentials [30,31]. Subjected to equidistant temperature quenches, these systems show asymmetry in relaxation: for a pair of thermodynamically equidistant temperature quenches, one from a lower and the other from a higher temperature, the relaxation at the ambient temperature is faster in the case of the former. Again, this situation is different from the one considered in the present paper.

II. MODEL AND METHODS

We consider an ideal gas contained between parallel, infinite planes separated by the distance L in the x direction (Fig. 1). The space between walls is filled with N moles of monatomic ideal gas per unit surface area.

Initially, the system is prepared in the quiescent, nonequilibrium stationary state [Fig. 1(a)] in which the wall at $x = 0$ is kept at temperature T_0, and the wall at $x = L$ is kept at temperature $T_1 = T_0 + \frac{dT}{dx}L$, where $\frac{dT}{dx}$ is the prescribed temperature gradient. The initial stationary profiles are as follows: $T_{st}(x) = T_0 + \frac{dT}{dx}x$ for temperature, $p_{st} = p_0\Theta$ for pressure with

$$\Theta = \frac{dT}{dx}\frac{L}{T_0}\left[\ln\left(1 + \frac{dT}{dx}\frac{L}{T_0}\right)\right]^{-1}, \quad (1)$$

$\rho_{st}(x) = \rho_0\Theta/(1 + \frac{dT}{dx}\frac{x}{T_0})$ for density, and $v_{st} = 0$ for velocity (in the x direction). The total internal energy of the system per unit area is $U_{st} = U_0^{eq}\Theta$. $\rho_0 = Mp_0/(RT_0)$ is the density of equilibrium monatomic ideal gas at temperature T_0 and pressure p_0, where R is the gas constant and M is the molar mass. $U_0^{eq} = \frac{3R}{2M}L\rho_0T_0$ is the corresponding total equilibrium internal energy per unit area. None of the above depend on transport coefficients, i.e., viscosities μ, λ or thermal conductivity κ. However, in a stationary state, a constant heat flux $J_{st} = -\kappa\frac{dT}{dx}$ is present, which depends on κ.

We assume local thermodynamic equilibrium, which in one dimension is valid even in a condition as extreme as a blast [32–37]. In higher dimensions, local equilibrium is valid in the case of dilute gases with negligible interactions. Otherwise, a more appropriate form of conservation laws and equations of state should be considered. We model gas dynamics using the dimensionless (see Appendix A) set of mass, energy, and momentum conservation equations [21] (Appendix D),

$$\partial_t\rho + \partial_x(v\rho) = 0, \quad (2a)$$

$$\rho[\partial_t v + \partial_x v^2] = -\frac{3}{5}\partial_x p + \frac{(\frac{\lambda}{\mu} + 2)}{Re}\partial_x^2 v, \quad (2b)$$

$$\partial_t(\rho u) = -\partial_x(\rho uv) - \frac{2}{3}p\partial_x v$$
$$+ \frac{10(\frac{\lambda}{\mu} + 2)}{9Re}(\partial_x v)^2 + \frac{1}{Pr\,Re}\partial_x^2 T, \quad (2c)$$

together with dimensionless ideal gas equations of state,

$$p = \rho T, \quad u = T, \quad (2d)$$

which can be used to substitute temperature T for internal energy density u in conservation laws. Re and Pr are Reynolds and Prandtl numbers, respectively (see Appendix A). The space coordinate is scaled with the system size L, density ρ is scaled with ρ_0, and T_0 sets the scale for temperature T. We choose to scale time t with $\tau_c = L/c_0$, where c_0 is the speed of sound at T_0. Another timescale naturally appearing in the problem is associated with thermal diffusion, $\tau_d = \frac{3L^2p_0}{2\kappa T_0}$. It depends on the transport coefficient κ as opposed to τ_c. The relation between timescales τ_c and τ_d is given by Eq. (A1) in Appendix A. We use both timescales depending on the analyzed phenomena: τ_c is the appropriate timescale for thermal front analysis, while τ_d is a better choice for describing the thermal relaxation of the system lasting longer than τ_c. We focus on the situations when $\tau_c \ll \tau_d$, and we provide an example of what happens when this condition is not satisfied (Appendix C). The further discussion features dimensionless quantities only. The dimensionless parameters used in our numerical calculations can be expressed as ratios of dimensional quantities, which can be inferred from observables of a physical realization of the system under consideration—see Appendix A. Our choice gives $\tau_d/\tau_c = 6 \times 10^3$ so that both timescales are well separated.

We performed numerical simulations with the OPENFOAM library for solving partial differential equations with the finite volume method [38–40]. We provide the necessary resources to reproduce the results (Appendix D). To ensure that the presented results are numerically accurate, we performed time integration for two time steps that differ tenfold and obtained indistinguishable results. Moreover, an agreement with the presented analytical solutions shows that the problem is also correctly resolved in terms of spatial dependencies.

III. CHANGES IN INTERNAL ENERGY

A. Approximations and full solution

The system is set out of nonequilibrium stationary state by changing the boundary conditions (b.c.) at the hotter wall from the fixed temperature $T_1 = 1 + \frac{dT}{dx}$ to adiabatic b.c. $\frac{dT}{dx}|_{x=1} = 0$ [Fig. 1(b)], which physically means ceasing the heat influx. In response, the heat outflux (set by the temperature gradient) through the colder wall does not change immediately, because information about events happening at the hotter wall needs time to reach the other wall. The total internal energy in the system at time t is

$$U(t) = \int_0^1 u(t)\rho(t)dx. \quad (3)$$

However, it is more convenient to discuss $U_{st} - U(t)$, which is the energy outflowing from the system at time t normalized with excess energy (over the equilibrium one U_0^{eq}) of
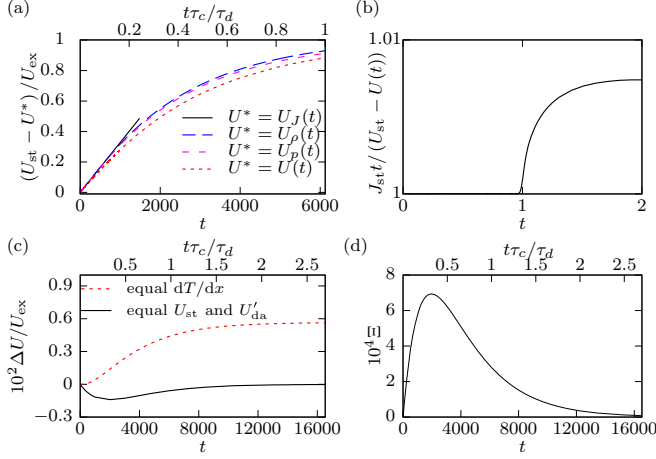
FIG. 2. Internal energy as a function of time. (a) The solid black line shows the constant flux approximation, the blue extended dashed line shows the constant density approximation, the magenta short dashed line shows the constant pressure approximation, and the red dotted line shows the full solution results. The upper time axis shows time in units of τ_d. (b) Ratio of outflown internal energy due to the constant flux approximation to the full solution. (c) Asymmetry between energy influx and outflux. The difference between instantaneous dearth and excess energy in the heating and cooling process to different end temperatures but with the same initial temperature gradient (dashed red line) as compared to the case of heating and cooling to the same end temperatures but with different initial temperature gradient and $U_{da'} = U_{ex}$ (solid black line). (d) Difference between relative outflown energy $\Xi(t)$ for temperature gradients $2\frac{dT}{dx}$ and $\frac{dT}{dx}$. Parts (c) and (d) are results of the full solution.

the stationary state $U_{ex} = U_{st} - 1$ (in units of U_0^{eq}) [41,42] [Fig. 2(a)]. With such a choice of normalization, $U_{st} - U(t)$ varies between 0 and 1.

We calculate the total internal energy $U(t)$ from Eq. (2) numerically and make a comparison with results obtained using three different approximations. The first is the stationary flux approximation, according to which the energy change when approaching equilibrium is governed by the (constant) heat flux at the initial stationary state, i.e.,

$$\frac{dU_J}{dt} = -J_{st}, \quad U(t=0) = U_{st} \rightarrow U_J = U_{st} - J_{st}t. \quad (4)$$

As one can expect, this linear decrease in energy is valid at the beginning of the relaxation process. The other two approximations are based solely on diffusive heat transport. The solution $U_\rho(t)$ assumes constant density equal to ρ_0 and no flow, $\mathbf{v} = \mathbf{0}$. Under this assumption, Eqs. (2) reduce to a simple heat conduction problem, which has an analytical solution [6]. The other solution is $U_p(t)$, which assumes only $\mathbf{v} = \mathbf{0}$ (Appendix D) resulting in $p = $ const. in each time instant. Within this approximation, the system is always able to relax to the state with a nonuniform density profile. In the presented example involving base parameters, $U_\rho(t)$ and $U_p(t)$ are indistinguishable until roughly $0.3\tau_d$, when half of the excess heat left the system. We observe that in the purely diffusive scenario, the heat flow is indistinguishable from linear one, as long as the changes in the temperature profile due to diffusion remain insignificant on the colder wall. Both

approximations follow the stationary flux approximation until roughly $0.15\tau_d$, when 30% of excess heat has already left the system. The full solution $U(t)$ of Eq. (2) diverges from the stationary flux approximation at τ_c [Fig. 2(b)] and gradually deviates from diffusive approximations. The difference is 10% in absolute excess heat after $0.5\tau_d$ [see Fig. 2(a)], which corresponds to approximately 20% relative difference. The presented numerical values depend on the system's parameters, i.e., they increase with $\frac{dT}{dx}$.

B. Asymmetries and Mpemba effect

One can stop the heat flux also at the colder wall, which raises a question about the symmetry between heating and cooling processes. Again, the perfect gas is initially between temperature 1 and T_1. If the hotter wall is set adiabatic, the system will cool down to the temperature of 1, and the total excess energy, which will flow out of the system, is

$$U_{ex} = U_{st} - 1 = \frac{T_1 - 1}{\ln[1 + (T_1 - 1)]} - 1. \quad (5)$$

It is not the same as the total dearth energy,

$$U_{de} = U_1^{eq} - U_{st} = T_1\left(1 - \frac{(1 - T_1)/T_1}{\ln[1 + (1 - T_1)/T_1]}\right), \quad (6)$$

which will flow into the system when the colder wall is set adiabatic and the system will heat up to the temperature of T_1. U_1^{eq} denotes the equilibrium energy at temperature T_1. Because the logarithm is convex, $U_{ex} < U_{de}$. For the heating process we define the instantaneous dearth $U_{de}(t) = U(t) - U_{st}$ energy, and for the cooling process we define the instantaneous excess $U_{ex}(t) = U_{st} - U(t)$ energy. Next, we consider a difference ΔU of these energies (normalized with stationary excess energy U_{ex}) as a function of time. The dashed line in Fig. 2(c) shows ΔU calculated for the base set of parameters. It grows slowly due to a mismatch between total excess and dearth energies. The initial vanishing slope indicates that both processes proceed at the same pace at the beginning. This is because the initial gradient is the same for both cases. The end value is $\Delta U \approx 0.56\%$. Additionally, cooling is faster than heating. It takes the base system $2.43\tau_d$ to expel 99.5% of U_{ex}. If we make the colder wall adiabatic, it takes $2.44\tau_d$ to intake 99.5% of U_{de}. Thus, the relative time difference is $0.01/2.43 \approx 0.4\%$ at the moment of 99.5% excess heat outflux. This difference increases with an imposed initial temperature gradient.

It is also interesting to compare times of cooling and heating to the *same* end temperature (equal to 1) when the excess energy is equal to the dearth energy. For this purpose, we consider a second system, in which the hotter wall has temperature 1 and the temperature at the colder wall T_0' is adjusted such that the dearth energy U_{de}' that will enter the system after making this wall adiabatic is equal to U_{ex} given by Eq. (5). One can show that T_0' has to satisfy

$$1 - \frac{T_0' - 1}{\ln[1 + (T_0' - 1)]} = \frac{T_1 - 1}{\ln[1 + (T_1 - 1)]} - 1. \quad (7)$$

The solution has the general property that $1 - T_0' < T_1 - 1$. Therefore, the initial temperature gradient, and hence the heat flux, are smaller in this (cooler) stationary state (with the

energy U'_{st}) as compared to the previously considered stationary state. In Fig. 2(c) we show by the solid line the difference ΔU between the instantaneous dearth and excess energies for this case. For the base set of parameters, $T'_0 = 288.028$, which gives the heat flux in the stationary state that is 0.56% smaller than the heat flux in the stationary state of the previous system. This is why we observe an initial decrease of ΔU for $U'_{de}(t)$. At the end of the relaxation process, ΔU goes to 0. Finally, for this colder system it takes $2.45\tau_d$ until 99.5% of U'_{de} is reached, which is longer than it takes the base system ($2.43\tau_d$) to expel 99.5% of U_{ex}.

In summary, if the temperature gradient in the initial steady states is the same, then the energy difference between the steady state and the final equilibrium (at different temperatures) controls the energy relaxation rate, i.e., the smaller this difference is, the faster is the process. If, on the other hand, the temperature gradients in the initial steady states are different, but the final equilibrium temperature is the same and, furthermore, the energy differences between the steady state and equilibrium are the same, the initial temperature gradient regulates the energy relaxation rate, i.e., the larger the gradient is, the faster is the relaxation process.

Next, we comment on the cooling rate as a function of the initial temperature gradient in relation to the Mpemba effect. We notice that $U_{ex} = \Theta - 1$ grows slower than linear with $\frac{dT}{dx}$ while the heat flux initially flowing through the system $-\frac{1}{\mathrm{Pr\,Re}}\frac{dT}{dx}$ is linear in $\frac{dT}{dx}$. This suggests that the analog of the Mpemba effect might occur. We introduce

$$\Xi(t) = \frac{U^{(1)}(t) - U^{(1)}_{st}}{U^{(1)}_{ex}} - \frac{U(t) - U_{st}}{U_{ex}}, \qquad (8)$$

a difference between relative energies flowing out from the system during cooling [Fig. 2(d)] for two different initial temperature gradients. Here, the superscript "(1)" denotes values for the system initiated with $2\frac{dT}{dx}$ and otherwise the same as the base system. We can see a small but persistent positive value of this function, which indicates that the hotter system (with a larger initial temperature gradient) cools faster.

C. Timescale analysis

As already pointed out [Fig. 2(b)], a deviation between the stationary approximation and the full solution occurs on a timescale comparable with τ_c. Immediately after changing b.c. on the hotter wall, a simultaneous appearance of diffusion effects and a traveling front can be seen in the temperature profile [Figs. 3(a) and 3(b)]. The diffusive process builds a gradual deviation from the stationary profile, which propagates from the hotter wall. At the same time, the traveling front lowers the temperature throughout the system by a small amount compared to the local field values in the stationary state.

For times longer than τ_c, the heat outflux differs from the stationary approximation [Figs. 2(a) and 2(b)], which must follow from the change in $\frac{dT}{dx}$ at the colder wall. This change cannot be caused by diffusion because this process is too slow to reach this wall so early in time. What we observe is the traveling front, which reflects multiple times from the walls and by each reflection reduces the temperature in the entire system by a small value. As a result, in the central part of the system, the temperature profile shifts downwards [Fig. 3(c)
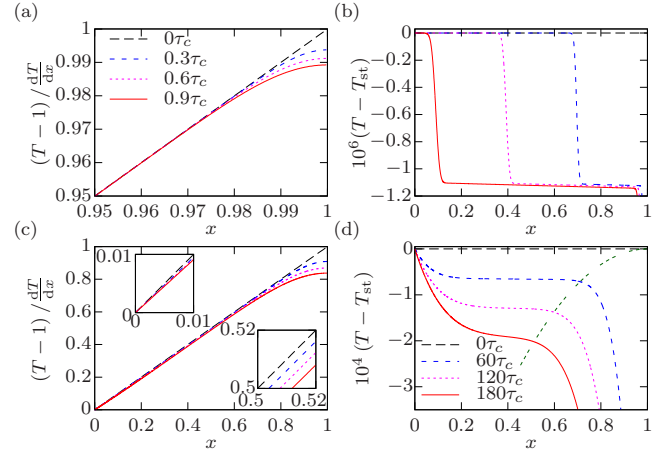

FIG. 3. Temperature profiles from the full numerical solution. On short timescales: (a) with respect to equilibrium temperature normalized with the temperature change $\frac{dT}{dx}$ in a stationary state, (b) with respect to $T_{st}(x)$. On longer timescales: (c) with respect to to equilibrium temperature normalized with the temperature change $\frac{dT}{dx}$ in a stationary state, (d) with respect to $T_{st}(x)$. The green triple dotted line illustrates the range of diffusion x_d.

and right inset]. Spanning from the walls, there are two parts of the system, which enlarge in time, showing a qualitative difference in behavior [Fig. 3(d)]. In part near the cold wall, the temperature approaches 1 with a slope smaller than the slope of the initial linear stationary profile [upper inset in Fig. 3(c)]. The part near the adiabatic wall shows a different deviation from the initially linear profile attributed to classical Fourier heat diffusion. For illustration purposes, we plotted a parabola showing the range of diffusion $x_d \propto t^{1/2}$, with a numerically determined proportionality coefficient. This visualization is possible as each front transition, to an excellent approximation, lowers the temperature profile by a constant value in τ_c.

IV. HEAT FRONT

A. General case

To analyze the traveling front, we postulate the solution in the following form (as suggested by the results of numerical simulations): $p(x) = p_{st} + \tilde{p}(x)$, $T(x) = T_{st}(x) + \tilde{T}(x)$, $\rho(x) = \rho_{st}(x) + \tilde{\rho}(x)$, and $v(x) = \tilde{v}(x)$, which includes small perturbations $\tilde{f} \ll f_{st}$ to the stationary state. We have solved (details in Appendix B) to the leading order Eq. (2) for small perturbations that have the form of a traveling front, $\tilde{f}(\chi) = \tilde{f}(x + v_w t)$. The front propagation velocity v_w is in the negative direction along the x axis, as in the simulations. We have found that for large Re,

$$v_w = c^* = \sqrt{\frac{p_{st}}{\rho^*_{st}}}, \qquad (9)$$

which is the speed of sound c^* at the position of the front x^*, and ρ^*_{st} is the stationary density at x^* (see Appendix B). Moreover, to the leading order, changes in pressure, density, temperature, and velocity are related by

$$\frac{\tilde{\rho}}{\rho^*_{st}} = \frac{3}{5}\frac{\tilde{p}}{p_{st}} = \frac{3}{2}\frac{\tilde{T}}{T_{st}} = -\frac{\tilde{v}}{c^*}. \qquad (10)$$
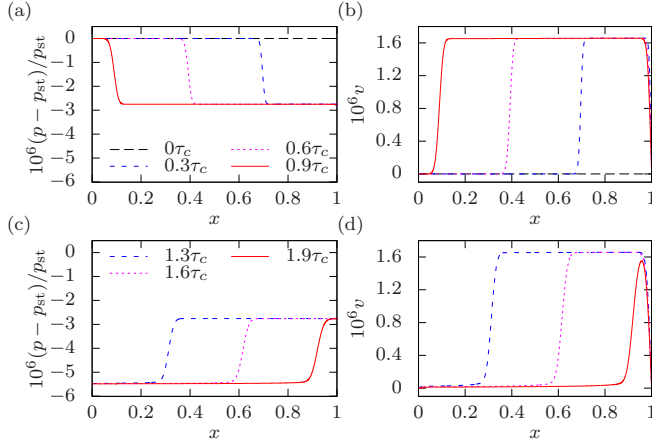
FIG. 4. Pressure and velocity profiles upon reflection obtained from the full numerical solution. (a) Pressure profile motion downstream heat flux before reflection at the wall. (b) The same as in (a) for the velocity profile. (c) Pressure profile motion upstream heat flux after reflection. (d) The same as in (b) for the velocity profile.
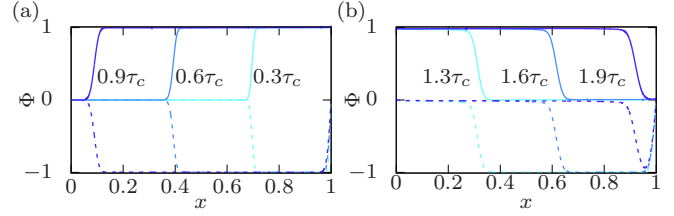

FIG. 5. Energy fluxes Φ normalized with stationary heat flux $\frac{1}{\mathrm{Pr\,Re}}\frac{dT}{dx}$. Solid lines correspond to the $\Phi = -\tilde{p}c^*$ component and dashed lines to the $\Phi = -\frac{5}{3}p_{\mathrm{st}}\tilde{v}$ component at consecutive time instances [see Eqs. (12) and (14)]. (a) Flux profiles before reflection at the wall. (b) Flux profiles after reflection at the wall plotted with respect to the state after the first front passage.

To demonstrate an excellent agreement between numerical results and analytically obtained relations (10), we quote the values obtained in numerical simulations for $t = 0.9$ and $x = 0.5$ normalized in the same way as in relations (10): $T - T_{\mathrm{st}} = 1.11 \times 10^{-6}$ (which corresponds to $\frac{\tilde{T}}{T_{\mathrm{st}}}$), $p - p_{\mathrm{st}} = 2.75 \times 10^{-6}$, $\rho - \rho_{\mathrm{st}} = 1.64 \times 10^{-6}$, and $v = 1.65 \times 10^{-6}$.

We supplement the profiles for temperature [Fig. 3(b)] with pressure and velocity profiles [Figs. 4(a) and 4(b)]. Upon reaching the wall, the pressure, temperature, and density profiles behave alike. Before contact, the front propagates in the direction of heat flux [Fig. 4(a)] leaving behind the gas in motion $\tilde{v} \neq 0$. After reaching the wall, the front reflects and propagates back, maintaining the jump magnitude [Fig. 4(c)] and bringing gas to rest again. With constant pressure, linear temperature profile, and zero velocity, the gas is again in a nonequilibrium stationary state, however different from the initial one. The situation repeats itself, resulting in a stepwise lowering of the profiles of thermodynamic parameters. At the same time, we observe that gas is alternately either at rest or moving [Figs. 4(b) and 4(d)]. The velocity of the gas is small in comparison with the speed of sound, which means that the kinetic energy density $\frac{\rho v^2}{2}$ is minuscule in comparison to the thermal energy density $\rho u = \frac{3p}{2}$.

We note that the leftmost equation (10) is a characteristic feature of the adiabatic process $\frac{d\rho}{\rho} = \frac{3}{5}\frac{dp}{p}$ for a monatomic ideal gas at fixed mass. This means that there is no change in entropy at the front. Indeed, the increment of the entropy (per mass density) $\tilde{s}$ across the front can be calculated using the expression for the change in entropy of an ideal gas (per mass) as follows:

$$\frac{R}{M}\left(\frac{5}{2}\ln\frac{T_{\mathrm{st}}+\tilde{T}}{T_{\mathrm{st}}} - \ln\frac{p_{\mathrm{st}}+\tilde{p}}{p_{\mathrm{st}}}\right)$$
$$= \frac{R}{M}\left(\frac{5}{2}\frac{\tilde{T}}{T_{\mathrm{st}}} - \frac{\tilde{p}}{p_{\mathrm{st}}}\right) + \cdots. \qquad (11)$$

Thus, to the leading order we have $\left(\frac{5}{2}\frac{\tilde{T}}{T_{\mathrm{st}}} - \frac{\tilde{p}}{p_{\mathrm{st}}}\right) = \tilde{s}$ and consequently $\tilde{s} = 0$.

Although the relations between changes in pressure, density, and entropy over the front are typical for the adiabatic process, in which there is no exchange of heat with surroundings, we observe the opposite, namely a depletion of the internal energy of the system. This depletion drives the front, leaving behind lower temperature, pressure, and density. Such behavior is unlike sound waves [17] or shock [18–20,43,44], where the energy is conserved during the transition of the disturbance.

Based on our numerical solution, we made an interesting observation regarding the relation between the change of the internal energy density $\rho u - \rho_{\mathrm{st}}u_{\mathrm{st}}$ at the front and the negative change of heat flux (from the stationary value $-\frac{1}{\mathrm{Pr\,Re}}\frac{dT}{dx}$ to 0), which we enforced by modifying b.c. This relation can be written as

$$-\frac{1}{\mathrm{Pr\,Re}}\frac{dT}{dx} = \tilde{p}c^*. \qquad (12)$$

We confirm this observation by reconstructing the front analytically for a special case below. Equation (12) can be interpreted as the equality of propagation speeds of information about the change in flux and its effect.

As a consequence of the equality (12), after passing of the front, the total internal energy flux should be equal to zero. Thus, in order to satisfy the energy conservation given by Eq. (2c), the flux that is supported by the local temperature gradient behind the front has to be balanced by other types of fluxes acting in the opposite direction:

$$\frac{1}{\mathrm{Pr\,Re}}\frac{dT}{dx} = \rho T v + \frac{2}{3}pv. \qquad (13)$$

After expanding to the leading order and utilizing the constitutive relations, we find

$$\frac{1}{\mathrm{Pr\,Re}}\left(\frac{dT}{dx} + \partial_x\tilde{T}\right) = \frac{5}{3}p_{\mathrm{st}}\tilde{v}. \qquad (14)$$

In this way, we obtained the relation between $\tilde{v}$, $\partial_\chi\tilde{T}$ ($\partial_\chi = \partial_x$), and $\frac{dT}{dx}$ behind the front. Often the $\partial_\chi\tilde{T}$ term can be discarded as introducing smaller order correction to $\tilde{v}$. The heat flux decomposition into two components before reflection from the wall is illustrated in Fig. 5(a). The increase in internal
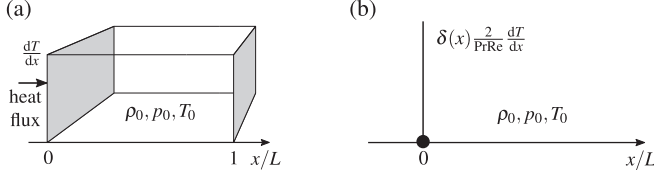
FIG. 6. Finite and infinite setup equivalent for $t < \tau_c$. (a) Finite system initialized in the equilibrium state, with heat flux introduced at the boundary. (b) Infinite system initialized in the equilibrium state with heat flux introduced as a point source.

energy density multiplied by the front velocity equals the stationary heat flux. At the same time, the convected energy has the same magnitude and the opposite direction and leaves zero net flux of internal energy behind the front. The front, moving in the direction of heat flux, leaves gas flowing in the opposite direction, which is impossible if the front is adiabatic in the same sense as shock or sound waves (fluid mechanics [18]). After reflection, the front again lowers all thermodynamic parameters by a discrete amount [Fig. 5(b)]. In the leading order, changes introduced by the second swipe are the same as in the first one. The gas is immobilized in a process symmetric to the initial front passage, and flux of internal energy is again supported primarily by heat flux while convective processes cease. Thus, the macroscopic movement of gas results from heat flux balance satisfying energy conservation. Because of linearity, the presented results are valid for an arbitrary change in heat flux, which we illustrate in Appendix C.

B. Special case and hydrodynamic modes

We investigate the properties of the front in more detail by analyzing analytically a special case when the system is initially in equilibrium: with $T_0 = T_1 = 1$, $\rho_0 = \rho_1 = 1$, and $p_0 = p_1 = 1$ as shown in Fig. 6(a). We introduce a constant heat flux $J = -\frac{1}{\text{Pr Re}}\frac{dT}{dx}$ to the system by setting a fixed nonzero gradient of temperature $\frac{dT}{dx}$ at the wall at $x = 0$. We are interested only in the front properties. Therefore, we map a finite system with a flux at the boundary into a one-dimensional infinite system with a heat source $2\delta(x)\frac{1}{\text{Pr Re}}\frac{dT}{dx}$ at the center of the reference frame, where $\delta(x)$ is Dirac's delta distribution [Fig. 6(b)]. The multiplication by 2 results from heat flux going to both sides of the point source compared to a single side for the wall. For such a configuration, the linearized Eqs. (2) become

$$\partial_t \tilde{\rho} = \partial_x \tilde{v} - \delta(x)\frac{2}{\text{Pr Re}}\frac{dT}{dx}, \tag{15a}$$

$$\partial_t \tilde{v} = -\frac{3}{5}\partial_x \tilde{p} + \frac{4}{3\,\text{Re}}\partial_x^2 \tilde{v}, \tag{15b}$$

$$\partial_t \tilde{p} = -\frac{5}{3}p_{\text{st}}\partial_x \tilde{v} + \frac{1}{\text{Pr Re}}\partial_x^2(\tilde{p} - \tilde{\rho}) + \delta(x)\frac{2}{\text{Pr Re}}\frac{dT}{dx}. \tag{15c}$$

For the small disturbances around the equilibrium, we substituted the temperature change with the pressure change minus the density change according to the equation of state. Equations (15) can be solved using a Fourier transform in space (q

is the conjugate of x), which is standard procedure when discussing hydrodynamic modes (see [45], Chap. 5). The novelty comes from the heterogeneous component, which fortunately allows for full analytical solution. It is spanned by the classical hydrodynamic modes: heat diffusion and damped sound wave propagation. They correspond to the following eigenvectors:

$$\phi_1 = \begin{pmatrix} 1 \\ 0 \\ 0 \end{pmatrix}, \quad \phi_2 = \begin{pmatrix} 1 \\ 1 \\ 5/3 \end{pmatrix}, \quad \phi_3 = \begin{pmatrix} 1 \\ -1 \\ 5/3 \end{pmatrix}, \tag{16a}$$

and eigenvalues

$$\lambda_1 = -\frac{3}{5\,\text{Pr Re}}q^2, \quad \lambda_{2,3} = -\frac{q^2}{\xi} \mp iq, \quad \xi = \frac{15\,\text{Pr Re}}{(10\,\text{Pr} + 3)}. \tag{16b}$$

The coordinates in the vector space are $(\tilde{\rho}, \tilde{v}, \tilde{p})$. From the structure of eigenmodes, we can see the timescale ξ at which viscous damping will blur the front. It acts quicker than thermal diffusion, but for small and moderate Prandtl numbers it is comparable. For a finite system, this suggests that on the timescale of thermal diffusive relaxation, the size of the front will become comparable to the size of the system. We now understand why we observe the front for hundreds of swipes in our numerical example. We deliberately chose parameters to pronounce timescale separations between diffusion and sound propagation.

The full solution to Eq. (15) is

$$\boldsymbol{\Psi}(\mathbf{x}, t) = c_1\phi_1 f_1(x, t) + c_2\phi_2 f_2(x, t) + c_3\phi_3 f_3(x, t) \tag{17a}$$

with the following coefficients:

$$c_1 = -\frac{4}{5}, \quad c_2 = \frac{3}{5\,\text{Pr Re}}\frac{dT}{dx}, \quad c_3 = \frac{3}{5\,\text{Pr Re}}\frac{dT}{dx} \tag{17b}$$

multiplying eigenvectors and functions

$$f_1(x, t) = \frac{\text{Pr Re}}{6}\left[5x\,\text{erf}\left(\frac{x}{2}\sqrt{\frac{5\,\text{Pr Re}}{3t}}\right) + 2\sqrt{\frac{15t}{\pi\,\text{Pr Re}}}e^{-\frac{5\,\text{Pr Re}x^2}{12t}} - 5x\right], \tag{17c}$$

$$f_2(x, t) = \frac{1}{2}\left[\text{erfc}\left(\frac{\sqrt{\xi}}{2}\frac{(x-t)}{\sqrt{t}}\right) - e^{\xi x}\text{erfc}\left(\frac{\sqrt{\xi}}{2}\frac{(x+t)}{\sqrt{t}}\right)\right], \tag{17d}$$

$$f_3(x, t) = \frac{1}{2}\left[e^{-\xi x}\text{erfc}\left(\frac{\sqrt{\xi}}{2}\frac{(x-t)}{\sqrt{t}}\right) - \text{erfc}\left(\frac{\sqrt{\xi}}{2}\frac{(x+t)}{\sqrt{t}}\right)\right]. \tag{17e}$$

The $\text{erf}(z) = \frac{2}{\sqrt{\pi}}\int_0^z e^{-\zeta^2}d\zeta$ is the error function and $\text{erfc}(z) = 1 - \text{erf}(z)$ is the complimentary error function. We show an excellent agreement of the heat front profiles obtained by the Fourier transform with the results of numerical simulations of the system with base parameters in Figs. 7(a)–7(d). From the linearity of the governing equations, we can say that our findings for the special case can be directly mapped to the stationary case discussed in the previous section as long as
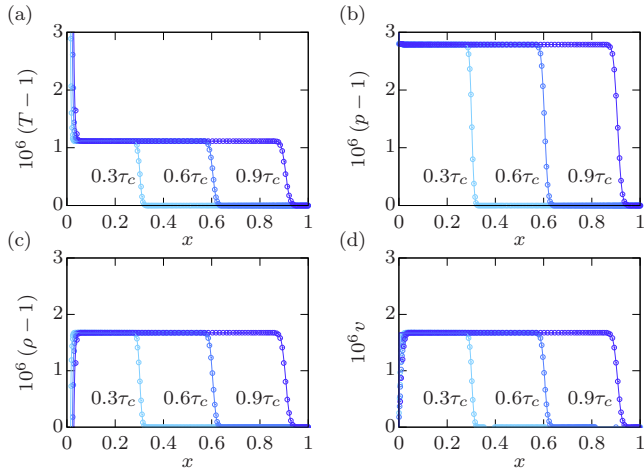
FIG. 7. Comparison of analytical (solid line) and numerical (circles) solutions for three time instances $(0.3\tau_c, 0.6\tau_c, 0.9\tau_c)$: (a) temperature, (b) pressure, (c) density, and (d) velocity.

the linearization procedure does not introduce significant errors. We discuss the front properties as a function of system parameters in Appendix C. In Appendix C, we also compare the situation when the system is driven out-of-equilibrium by setting a nonzero value of the temperature gradient on one wall with the situation in which the temperature on one wall is different from that on the other. We point out the significant differences between the solutions for these two situations.

V. CONCLUSIONS

We analyzed the heat transport in ideal gas during thermal relaxation from a nonequilibrium stationary state after turning off the heat flux (Fig. 1). We found a new mode of heat transport, which is present in addition to the diffusive temperature spreading [46], a front traveling with the local speed of sound (9). It reflects from the system's boundaries and upon each transition simultaneously decreases [cooling, Figs. 3(b) and 4] or increases (heating) all three thermodynamic parameters: temperature, density, and pressure without changing the entropy (11). Strangely, for cooling, the front travels toward higher pressure. During the front's transition, the gas undergoes a process similar to the adiabatic process but driven by the heat outflow. This is unlike sound waves [17] or shock [18–20,43,44]. The observed front is not a form of ballistic heat transport as no particles or phonons are involved. Also, the front is not a heat wave [47,48], which decays exponentially over a characteristic lengthscale. We derive the analytical structure of the front [Eqs. (17)] to stress the difference between waves, shocks, and ballistic heat transport reported in the literature to date. The essential feature is the change in the heat flux passing through the system. The front structure is similar to the reaction-diffusion systems and not for wave or diffusion equations.

The front causes large parts of the system to transit between well-separated (quantized) stationary states. The distance between those states in the space of thermodynamic functions can be determined to the leading order by comparing the change in the heat flux with the change in local energy density

propagating with the local speed of sound [see Eq. (9)]. The swipes of the front induce high-frequency oscillations in the gas velocity [Figs. 4(b) and 4(d)] that have a small magnitude compared to the speed of sound (10). Consequently, every change in heat flux necessarily leads to macroscopic gas movement. We propose an interpretation of the front velocity as the heat velocity in the ideal gas.

As time approaches τ_d, diffusion becomes the dominant mode of changes in the system [Figs. 2(a) and 3(d)]. Before that happens, the front action modifies the timescale of energy exchange with the environment compared to pure diffusion. The front lowers the temperature throughout the system [Fig. 3(c)] reducing the gradient at the colder wall. As a result, the energy flows out of the system slower than in the purely diffusive case [Fig. 2(a)]. This depends on the ratio between τ_c and τ_d and the change in the initial flux. In the presented example, the slowing down in the outflow of 80% of available energy reaches roughly 25% of elapsed time.

The return to equilibrium exhibits asymmetry [Fig. 2(c)] and the system cools down quicker than it heats up. We associate it with the relation between the energy stored in the system and the underlying heat flux. The increase in the heat flux is linear in the temperature difference, while the excess energy grows slower than linear. As a result, we found that the hotter system cools down quicker, which is the analog of the Mpemba effect [Fig. 2(d)]. It would be interesting to analyze this effect within the framework of nonequilibrium thermodynamics. However, this requires additional numerical simulation, and we leave it for future studies.

In our opinion, the presented results can be generalized to more realistic systems, but further research must confirm this. Here, we can only speculate on the effects of releasing assumed constraints. For example, changing geometry from an infinite slab to a channel will influence the results quantitatively, but we expect the qualitative results to prevail. In the case of total energy outflux, the fundamental reason for the asymmetry is the difference in functional dependence on the boundary conditions between the heat flux and the amount of heat available for the exchange with the environment. The geometric details may modify but will not eradicate this difference. In the case of heat front, the jumps of thermodynamic properties will depend on the surface area of the front, which in turn depends on geometry. The ideal gas model is convenient computationally but has limited applications. The other models will introduce modifications into the conservation laws and need to be considered separately to resolve all possible additional features. However, we think it is unlikely that this introduces symmetry between cooling and heating. Also, the front results from propagating the cessation of the heat flux, which is present in energy conservation law regardless of its specific form. Therefore, it will be present with possibly modified properties.

The experimental observation of the phenomenon described in this paper is difficult but feasible. At the moving front, the temperature drops and its change can be monitored by an array of thermocouples placed at micrometer spacing, as was done by Fang and Ward in the study of the evaporation phenomena [49,50]. However, it can be challenging to build a wall that can instantly change from heat-conducting to adiabatic.

APPENDIX A: RESCALING AND PARAMETERS OF THE MODEL

The space coordinate is scaled with the system size L, while density ρ with ρ_0 and T_0 sets the scale for temperature T. Time t is scaled with $\tau_c = L/c_0$, where $c_0 = \sqrt{\gamma \frac{RT_0}{M}}$ is the speed of sound at T_0, and the coefficient $\gamma = c_p/c_V$ is the ratio of specific heat at constant pressure to specific heat at constant volume. For monatomic ideal gas, $c_V = 3R/(2M)$ and $\gamma = 5/3$. Consequently, c_0 sets the velocity v scale and $\partial_x T$ is in units of T_0/L. The pressure p is scaled with the equilibrium pressure $p_0 = \frac{\rho_0 T_0 R}{M}$, while the internal energy per mass unit u is given in the equilibrium units $u_0^{\text{eq}} = c_V T_0$. The dimensionless numbers are Re $= \frac{\rho_0 L c_0}{\mu}$ (Reynolds), Pr $= \frac{\mu c_V}{\kappa}$ (Prandtl), which include thermal conductivity κ, and $\frac{\lambda}{\mu}$ (gas viscosities ratio). In the case of monatomic gas, zero bulk viscosity is widely accepted [51,52], which gives $\lambda = -2\mu/3$.

Another timescale naturally appearing in the problem is associated with thermal diffusion, $\tau_d = \frac{L^2 c_V \rho_0}{\kappa} = \frac{3L^2 p_0}{2\kappa T_0}$. It depends on the transport coefficient κ contrary to τ_c. The ratio

$$\tau_c/\tau_d = \frac{2\kappa (M)^{1/2}}{3L p_0 (\gamma R T_0)^{1/2}} \tag{A1}$$

increases with κ and decreases with system size, pressure, and temperature.

All our numerical results have been calculated using the following (base) set of parameters: $T_0 = 293$ K, $\frac{dT}{dx}\frac{L}{T_0} = 5/293$, $p_0 = 101\,325$ Pa, molecular mass of helium $M = 4.0026 \times 10^{-3}$ kg/mol, constant viscosity $\mu = 1.8805 \times 10^{-5}$ Pa s, and Prandtl number Pr $= 0.6865$. The equilibrium parameters are close to standard conditions. For the base set of parameters, $c_0 = 1007.5$ m/s and $\rho_0 = 0.1665$ kg/m^3. The size of the base system is $L = 1$ mm, which gives

$$\tau_c = 10^{-6} \text{ s}, \quad \tau_d = 6 \times 10^{-3} \text{ s} \tag{A2}$$

and Reynolds number Re ≈ 8919.

APPENDIX B: HEAT FRONT SOLUTION

We discard higher-order terms and use the constitutive relation $p = \rho T$ in the energy conservation to obtain the ordinary differential equations for small perturbations,

$$\partial_t \tilde{\rho} + \partial_x (\rho_{\text{st}} \tilde{v}) = 0, \tag{B1a}$$

$$\rho_{\text{st}} \partial_t \tilde{v} = -\frac{3}{5} \partial_x \tilde{p} + \frac{4}{3\,\text{Re}} \partial_x^2 \tilde{v}, \tag{B1b}$$

$$\partial_t \tilde{p} = -\frac{5}{3} p_{\text{st}} \partial_x \tilde{v} + \frac{1}{\text{Pr Re}} \partial_x^2 \tilde{T}. \tag{B1c}$$

Next, we seek the solution in the form of a traveling front $\tilde{f}(\chi) = \tilde{f}(x + v_w t)$, where v_w is the velocity of front propagation in the negative direction along the x axis (the same direction as in simulations). In the full numerical solution, the front is not steplike but has its intrinsic width 2δ localized around its position x^*. We assume that a change in ρ_{st} over 2δ from $x^* - \delta$ to $x^* + \delta$ is negligible and equal to the value at the position of the front, $\rho_{\text{st}}^* = \rho_{\text{st}}(x^*)$. Subsequently, we integrate the equations between $\chi_1 = x^* - \delta$ and $\chi_2 = x^* + \delta$, with the b.c.: no perturbation before the front $\tilde{f}(x^* - \delta) = 0$ and a small perturbation after the front $\tilde{f}(x^* + \delta) = \tilde{f}$. These result in

$$v_w \tilde{\rho} + \rho_{\text{st}}^* \tilde{v} = 0, \tag{B2a}$$

$$v_w \rho_{\text{st}}^* \tilde{v} = -\frac{3}{5} \tilde{p} + \frac{4}{3\,\text{Re}} \partial_\chi \tilde{v}, \tag{B2b}$$

$$v_w \tilde{p} = -\frac{5}{3} p_{\text{st}} \tilde{v} + \frac{1}{\text{Pr Re}} \partial_\chi \tilde{T}. \tag{B2c}$$

The continuity equation can be rewritten as

$$\frac{\tilde{v}}{v_w} = -\frac{\tilde{\rho}}{\rho_{\text{st}}^*}. \tag{B3}$$

Similarly, the energy conservation equation can be written as

$$\frac{\tilde{v}}{v_w} = -\frac{3}{5} \left(\frac{\tilde{p}}{p_{\text{st}}} - \frac{1}{\text{Pr Re}} \frac{\partial_\chi \tilde{T}}{v_w p_{\text{st}}} \right). \tag{B4}$$

From momentum and energy conservation we obtain the quadratic equation for v_w that has a positive solution, which we expand in a series for small $1/\text{Re}$,

$$v_w = \sqrt{\frac{p_{\text{st}}}{\rho_{\text{st}}^*}} + \frac{1}{\text{Re}} \left[\frac{2\partial_\chi \tilde{v}}{3\rho_{\text{st}}^* \tilde{v}} - \sqrt{\frac{p_{\text{st}}}{\rho_{\text{st}}^*}} \frac{3\partial_\chi \tilde{T}}{10\,\text{Pr}\,p_{\text{st}} \tilde{v}} \right] + \cdots . \tag{B5}$$

For large Re and $\partial_\chi \tilde{T}$, $\partial_\chi \tilde{v}$ comparable to other variables, we find

$$v_w = c^* = \sqrt{\frac{p_{\text{st}}}{\rho_{\text{st}}^*}}, \tag{B6}$$

which is the speed of sound c^* at the position of the front x^*. However, in the general case the boundary conditions after the front passage for $\partial_\chi \tilde{T}$ and $\partial_\chi \tilde{v}$ are necessary.

APPENDIX C: ADDITIONAL RESULTS

1. Parameter dependence

We found that a characteristic steep increase over the front is present regardless of the simulation parameters. In Fig. 8 we show the change in pressure jump profile due to the modification of the value of a single parameter in relation to the base set. The increase of viscosity makes the front profile wider [Fig. 8(a)] as it increases the lengthscale of viscous relaxation. The increase of heat flux increases linearly the height of the front. It can be realized in two ways: either by increasing κ [Fig. 8(b)] or by increasing $\frac{dT}{dx}$ [Fig. 8(c)]. There is an important difference between modifying κ and $\frac{dT}{dx}$ to
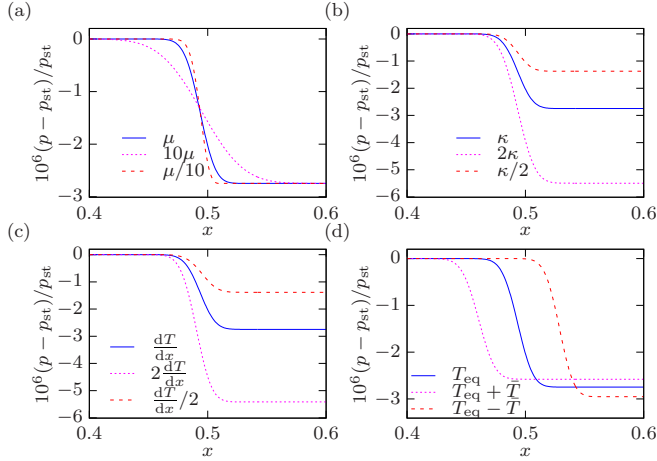
FIG. 8. Pressure profiles at $t = 0.5\tau_c$ (calculated with c_{eq}). Each panel shows changes due to modification of a single parameter. (a) Viscosity μ is changed by factor 10. (b) Thermal conductivity κ is changed by factor 2. (c) Temperature gradient $\frac{dT}{dx}$ is changed by factor 2. (d) Equilibrium temperature T_0 is changed by $\bar{T} = 40$ K.
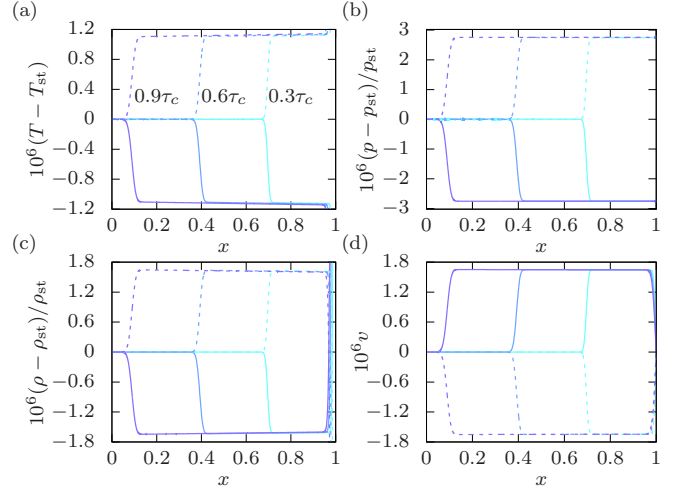

FIG. 9. Increasing heat flux. Solid lines denote solution with heat flux switched off, and dashed lines denote solution with doubled heat flux. (a) Temperature profile. (b) Pressure profile. (c) Density profile. (d) Velocity. The meaning of lines is the same for all panels.

change the flux. Modifying $\frac{dT}{dx}$ also influences the velocity of the traveling front and other features of the solution. In particular, it may take the solution out of the regime when changes in temperature gradient are negligible. The change in equilibrium temperature influences primarily the velocity of the traveling front [Fig. 8(d)]. This is manifested by a difference in the front position at the same moment in time, as well as a change in the size of the jump.

2. Arbitrary change in heat flux

Instead of switching off the heat flux, one can increase it, e.g., twofold. As a result, the traveling front has a jump of the opposite sign, but the derived relations in jump magnitudes are preserved (Fig. 9). The heat flux causes the temperature, pressure, and density to increase. The simultaneous increase in all three functions is possible because the front is triggered by the energy flux. Additionally, after the front has passed through, the gas flows in the direction of heat flux (Fig. 9).

In general, the magnitude of the front is governed by the change of heat flux ΔJ imposed on the boundary with respect to the stationary state,

$$\tilde{p}c^* = \Delta J. \tag{C1}$$

Another limiting case is the system in an equilibrium state in which no flux is present prior to the one introduced at the boundary.

3. Changing flux versus changing value at the boundary

We show the difference between forcing the system by changing the temperature or by introducing heat flux on the example of a system initially in the state of equilibrium. Initially we keep the system at T_0 and introduce either the constant heat flux [Fig. 10(a)] or constant temperature value [Fig. 10(b)] to the right boundary. Both result in the pulse traveling with the speed of sound, yet with very different char-

acteristics. When the temperature is raised to T_1, we observe a broadening peak that leaves elevated temperature behind. The constant flux results in a stepwise profile. However, to reach the comparable magnitude of the temperature increase, we used 60-times-higher flux that is present in the stationary state with T_1 at the right wall.

4. Long systems and large gradients

We present only a short and qualitative discussion of systems with large temperature gradients. We use an extreme example of a simulation in which $T_0 = 0.0001$ K, $p_{st} = 102\,187$ Pa (the same as in the base case), $T_1 = 586$ K, $L = 0.002$ mm, and the rest of the parameters are kept as in the base case. The characteristic time $\tau_c = 0.0034$ s, which is set by the speed of sound at very low equilibrium temperature. The Re number decreases like the square root of temperature and increases linearly with density. Thus, it can be very high and reaches $\approx 7 \times 10^5$ in the presented case. The dimensionless $\frac{dT}{dx} = 5.86 \times 10^6$, which is very large, and the ratio between it and Re (present in dimensionless flux $\frac{1}{\Pr \text{Re}} \frac{dT}{dx}$) is of the order of 10, which is much higher than
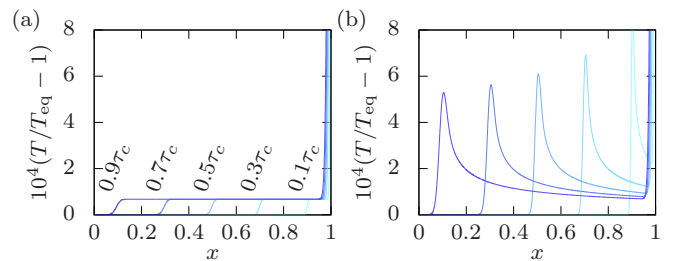

FIG. 10. Traveling pulse in the system initially in equilibrium temperature T_0 upon change of the boundary condition at the right wall to (a) constant dimensionless heat flux $J = 60$, (b) constant temperature T_1. The meaning of lines is the same for both panels.
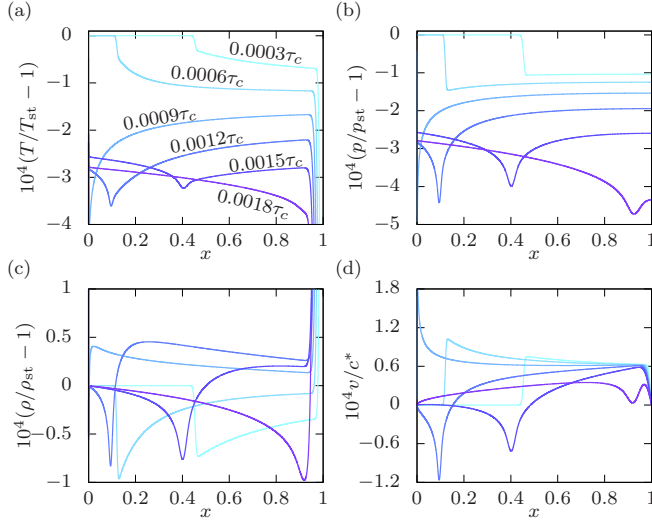
FIG. 11. Solution profiles for equally spaced time instances. (a) Temperature profile. (b) Pressure profile. (c) Density profile. (d) Velocity profile. The meaning of lines as denoted in (a) is the same for all panels.

in the case of a small gradient considered in the main text. These values may suggest also that other rescaling may be appropriate. The character of the solution changes when the front approaches the cold end of the system (Fig. 11). As a result, the jumps in profiles grow until reaching the wall. The reflection changes the profiles qualitatively. The temperature [Fig. 11(a)] and pressure [Fig. 11(b)] acquire a negative peak (dimple). The density increases with respect to the stationary state [Fig. 11(c)]. Finally, the velocity profile changes its sign [Fig. 11(d)]. This suggests that for very low temperatures, the diffusion and ballistic heat transport can no longer be treated separately.

APPENDIX D: NUMERICAL METHODS

1. Computational tool

Numerical simulations were performed using the open source library OPENFOAM [38–40], which was developed to solve partial differential equations with the finite volume method [53,54].

The complete set of equations is mass, momentum (with linear stress tensor, constant viscosity, and zero bulk viscosity), and energy conservation equations (with constant thermal conductivity) closed with the constitutive relations for monatomic ideal gas [21],

$$\frac{\partial \rho}{\partial t} + \nabla \cdot (\mathbf{v}\rho) = 0, \tag{D1a}$$

$$\rho \left[\frac{\partial \mathbf{v}}{\partial t} + \nabla \cdot (\mathbf{v}\mathbf{v}) \right] = -\nabla p - \nabla \cdot \mathbf{\Pi}, \tag{D1b}$$

$$\frac{3R}{2M} \frac{\partial \rho T}{\partial t} = -\nabla \cdot \left(\frac{3}{2} \frac{R}{M} \rho T \mathbf{v} \right) - p\nabla \cdot \mathbf{v}$$
$$- \mathbf{\Pi} : \nabla \mathbf{v} + \kappa \nabla \cdot \nabla T, \tag{D1c}$$

$$\mathbf{\Pi} = \frac{2}{3}\mu(\nabla \cdot \mathbf{v})\mathbf{I} - \mu\left(\nabla \mathbf{v} + (\nabla \mathbf{v})^{\mathrm{T}}\right), \tag{D1d}$$
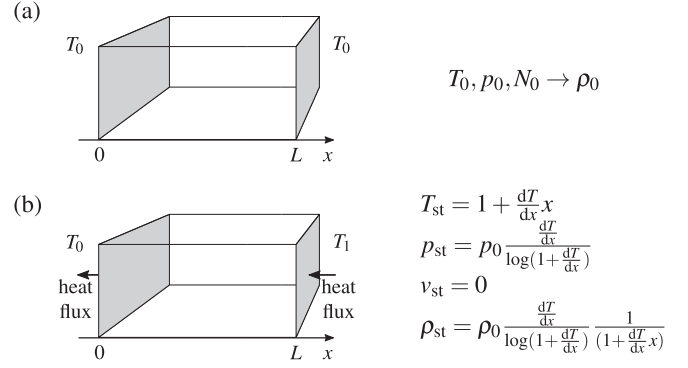

FIG. 12. Geometry, initial and boundary conditions. (a) System prepared in the equilibrium state. (b) System transformed from equilibrium to a stationary state.

$$p = \rho \frac{RT}{M}, \tag{D1e}$$

$$u = \frac{3}{2} \frac{RT}{M}. \tag{D1f}$$

In the above, ρ is density, t is time, $\mathbf{v}$ is velocity, p is pressure, $\mathbf{\Pi}$ is the dynamic part of the stress tensor, R is a gas constant, M is molar mass, κ is thermal conductivity, μ is viscosity, $\mathbf{I}$ denotes a unit tensor, and u is the internal energy per unit mass.

The equations are solved iteratively in a time loop with the PISO algorithm [55], which is used for solving the pressure-velocity coupling problem in the Navier-Stokes equation.

To compare the full solution with the diffusive solution, we solve the following reduced set of equations:

$$\frac{\partial \left(\int \rho \, d\mathbf{r} \right)}{\partial t} = 0, \tag{D2a}$$

$$\frac{3R}{2M} \frac{\partial \rho T}{\partial t} = \kappa \nabla \cdot \nabla T, \tag{D2b}$$

$$p = \rho \frac{RT}{M}, \tag{D2c}$$

$$u = \frac{3}{2} \frac{RT}{M}, \tag{D2d}$$

which is obtained from (D1) assuming $\mathbf{v} = \mathbf{0}$, $p = \text{const}$ and physically means that the total mass in the system is conserved and density will follow the temperature distribution immediately.

2. Geometry, boundaries, and initial conditions

Simulations were performed in one-dimensional geometry (along the x axis) that had length L and impermeable boundaries at $x = 0$ and $x = L$ [Fig. 12(a)]. The geometry was filled with N moles of ideal gas in such way that in thermal equilibrium at temperature T_0 under equilibrium pressure T_0, density is equal to equilibrium density ρ_{eq}. Next, the system was transformed to the stationary state given uniquely by T_0, $\frac{dT}{dx}$, and N moles of gas the same as in equilibrium [Fig. 12(b)]. We used for that purpose an additional utility written in OPENFOAM.

In the simulations, we used $L = 10^{-3}$ m, which was divided into 3000 computational cells that correspond to $1/3 \times 10^{-6}$ m. We found this spatial resolution sufficiently high to resolve the details of the traveling front, which had a lengthscale δ of 8×10^{-5} m (corresponding to roughly 240 computational cells). The velocity of sound in simulated gas (helium) was close to 10^3 m/s. In the simulations, we used the time step 10^{-11} and 10^{-12} s to be sure that we resolved all relative timescales correctly. Both time steps gave indistinguishable results.

3. Code availability

The OPENFOAM codes for solving Eqs. (D1) and (D2) together with application setting the initial conditions are available. They were written, used, and tested under a foam-extend 4.1 distribution. The package `DataS1.zip` includes the following:

(i) `eRhoFullFoam`—the OPENFOAM solver for solving Eqs. (D1).

(ii) `eRhoReducedFoam`—the OPENFOAM solver for solving Eqs. (D2).

(iii) `statInitLine`—the OPENFOAM utility to set stationary-state initial conditions.

(iv) `fullSolution`—the one-dimensional case including a traveling front.

(v) `reducedSolution`—the one-dimensional case including diffusive heat transport only.

(vi) `shortManual.pdf`—the short manual explaining the usage of the code.

The package can be downloaded from the github repository [56].

[1] L. Onsager, Phys. Rev. **37**, 405 (1931).

[2] L. Onsager, Phys. Rev. **38**, 2265 (1931).

[3] R. Kubo, M. Yokota, and S. Nakajima, J. Phys. Soc. Jpn. **12**, 1203 (1957).

[4] R. Kubo, *Thermodynamics: An Advanced Course with Problems and Solutions* (North-Holland, Amsterdam, 1976), Vol. 1.

[5] R. Hołyst and A. Poniewierski, *Thermodynamics for Chemists, Physicists and Engineers* (Springer, Dordrecht, 2012).

[6] H. S. Carslaw and J. C. Jaeger, *Conduction of Heat in Solids* (Oxford University Press, Oxford, 1986).

[7] J. C. Maxwell, Philos. Trans. R. Soc. London A **157**, 49 (1867).

[8] C. Cattaneo, Atti Del Semin. Matem. E Fis. Della Univ. Modena **3**, 83 (1948).

[9] P. M. Morse and H. Feshbach, Am. J. Phys. **22**, 410 (1954).

[10] P. Vernotte, C. R. Hebd. Acad. Sci. **247**, 2103 (1958).

[11] D. D. Joseph and L. Preziosi, Rev. Mod. Phys. **61**, 41 (1989).

[12] M. N. Özisik and D. Y. Tzou, J. Heat Transf. **116**, 526 (1994).

[13] J. Lombard, T. Biben, and S. Merabia, Nanoscale **8**, 14870 (2016).

[14] G. Chen, Phys. Rev. Lett. **86**, 2297 (2001).

[15] R. Yang, G. Chen, M. Laroche, and Y. Taur, J. Heat Transf. **127**, 298 (2005).

[16] J. Maassen and M. Lundstrom, J. Appl. Phys. **117**, 035104 (2015).

[17] P. M. Morse and K. U. Ingard, *Theoretical Acoustics* (McGraw-Hill, New York, 1968).

[18] L. D. Landau and E. M. Lifshitz, *Course of Theoretical Physics* (Elsevier/Butterworth-Heinemann, Amsterdam, 2006).

[19] Y. B. Zeldovich, Y. P. Raizer, W. D. Hayes, and R. F. Probstein, *Physics of Shock Waves and High-temperature Hydrodynamic Phenomena* (Academic, New York, 1967), Vol. 1.

[20] Y. B. Zeldovich, Y. P. Raizer, W. D. Hayes, and R. F. Probstein, *Physics of Shock Waves and High-temperature Hydrodynamic Phenomena* (Academic, New York, 1967), Vol. 2.

[21] S. R. De Groot and P. Mazur, *Non-equilibrium Thermodynamics* (Dover, New York, 1984).

[22] Aristotle, Meteorologica.

[23] E. B. Mpemba and D. G. Osborne, Phys. Ed. **4**, 172 (1969).

[24] A. Kumar and J. Bechhoefer, Nature (London) **584**, 64 (2020).

[25] I. Klich, O. Raz, O. Hirschberg, and M. Vucelja, Phys. Rev. X **9**, 021060 (2019).

[26] Z. Lu and O. Raz, Proc. Natl. Acad. Sci. (USA) **114**, 5083 (2017).

[27] A. Gal and O. Raz, Phys. Rev. Lett. **124**, 060602 (2020).

[28] A. Lasanta, F. Vega Reyes, A. Prados, and A. Santos, Phys. Rev. Lett. **119**, 148001 (2017).

[29] A. Biswas, V. V. Prasad, O. Raz, and R. Rajesh, Phys. Rev. E **102**, 012906 (2020).

[30] A. Lapolla and A. Godec, Phys. Rev. Lett. **125**, 110602 (2020).

[31] T. Van Vu and Y. Hasegawa, Phys. Rev. Research **3**, 043160 (2021).

[32] S. Ganapa, S. Chakraborti, P. L. Krapivsky, and A. Dhar, Phys. Fluids **33**, 087113 (2021).

[33] S. Chakraborti, S. Ganapa, P. L. Krapivsky, and A. Dhar, Phys. Rev. Lett. **126**, 244503 (2021).

[34] G. I. Taylor, Proc. R. Soc. London A **201**, 159 (1950).

[35] G. I. Taylor, Proc. R. Soc. London A **201**, 175 (1950).

[36] J. von Neumann, *Theory of Games, Astrophysics, Hydrodynamics and Meteorology* (Pergamon, Oxford, 1963), Vol. 6.

[37] L. I. Sedov, J. Appl. Math. Mech. **10**, 241 (1946).

[38] H. G. Weller, G. Tabor, H. Jasak, and C. Fureby, Comput. Phys. **12**, 620 (1998).

[39] H. Jasak, A. Jemcov, and Z. Tukovic, in *International Workshop on Coupled Methods in Numerical Dynamics* (IUC Dubrovnik, Croatia, 2007), Vol. 1000, pp. 1–20.

[40] Foam extend project, https://sourceforge.net/projects/foam-extend/.

[41] R. Holyst, A. Maciołek, Y. Zhang, M. Litniewski, P. Knychała, M. Kasprzak, and M. Banaszak, Phys. Rev. E **99**, 042118 (2019).

[42] Y. Zhang, M. Litniewski, K. Makuch, P. J. Żuk, A. Maciołek, and R. Hołyst, Phys. Rev. E **104**, 024102 (2021).

[43] W. J. M. Rankine, Philos. Trans. R. Soc. London **160**, 277 (1870).

[44] H. Hugoniot, J. Ec. Polyt. Paris **58**, 1 (1889).

[45] P. M. V. Résibois, M. De Leener, and M. F. De Leener, *Classical Kinetic Theory of Fluids* (Wiley, New York, 1977).

[46] B. Ahlborn and F. L. Curzon, J. Non-Eq. Thermodyn. **29**, 301 (2004).

[47] H. Vargas and L. C. M. Miranda, Phys. Rep. **161**, 43 (1988).

[48] E. Marín, in *Thermal Wave Physics and Related Photothermal Techniques: Basic Principles and Recent Developments*, edited by E. M. Moares (Transworld Research Network, Kerala, India, 2009), pp. 1–27.

[49] G. Fang and C. A. Ward, Phys. Rev. E **59**, 417 (1999).

[50] G. Fang and C. A. Ward, Phys. Rev. E **59**, 441 (1999).

[51] L. Tisza, Phys. Rev. **61**, 531 (1942).

[52] M. S. Cramer, Phys. Fluids **24**, 066102 (2012).

[53] R. Eymard, T. Gallouët, and R. Herbin, in *Handbook of Numerical Analysis*, edited by J. L. Lions and P. Ciarlet (Elsevier, New York, 2000), Vol. 7, pp. 713–1018.

[54] H. K. Versteeg and W. Malalasekera, *An Introduction to Computational Fluid Dynamics: The Finite Volume Method* (Pearson Education, Harlow, England, 2007).

[55] R. I. Issa, J. Comput. Phys. **62**, 40 (1986).

[56] https://github.com/pjzuk/heatFrontSData.git.